

Vol. 19 • No. 49 • December 6 • 2023

www.small-journal.com

NANO • MICRO small

WILEY-VCH

A Sewing Approach to the Fabrication of Eco/bioresorbable Electronics

Yunyun Wu, Eric Rytkin, Miles Bimrose, Shupeng Li, Yeon Sik Choi, Geumbee Lee, Yue Wang, Lichao Tang, Micah Madrid, Grace Wickerson, Jan-Kai Chang, Jianyu Gu, Yamin Zhang, Jiaqi Liu, Sameh Tawfick, Yonggang Huang, William P. King, Igor R. Efimov, and John A. Rogers*

Eco/bioresorbable electronics represent an emerging class of technology defined by an ability to dissolve or otherwise harmlessly disappear in environmental or biological surroundings after a period of stable operation. The resulting devices provide unique capabilities as temporary biomedical implants, environmental sensors, and related systems. Recent publications report schemes to overcome challenges in fabrication that follow from the low thermostability and/or high chemical reactivity of the eco/bioresorbable constituent materials. Here, this work reports the use of high-speed sewing machines, as the basis for a high-throughput manufacturing technique that addresses many requirements for these applications, without the need for high temperatures or reactive solvents. Results demonstrate that a range of eco/bioresorbable metal wires and polymer threads can be embroidered into complex, user-defined conductive patterns on eco/bioresorbable substrates. Functional electronic components, such as stretchable interconnects and antennas are possible, along with fully integrated systems. Examples of the latter include wirelessly powered light-emitting diodes, radiofrequency identification tags, and temporary cardiac pacemakers. These advances add to a growing range of options in high-throughput, automated fabrication of eco/bioresorbable electronics.

1. Introduction

Electronics technologies play a central role in nearly every aspect of modern society, with growing importance in monitoring human health and the status of our environment. Recent research establishes the foundations for eco/bioresorbable forms of electronics, defined by an ability to dissolve, disintegrate, enzymatically degrade, or otherwise harmlessly disappear in a natural environment or in the body, after a controlled lifetime. Applications range from transient pollution monitors that do not require recovery to temporary implants that avoid the need for surgical removal.^[1–7] Despite these unique and important opportunities, development of methods for mass manufacturing of such devices remains challenging. Traditional techniques used in the semiconductor industry, such as photolithography and wet etching, cannot be used without modification because many eco/bioresorbable

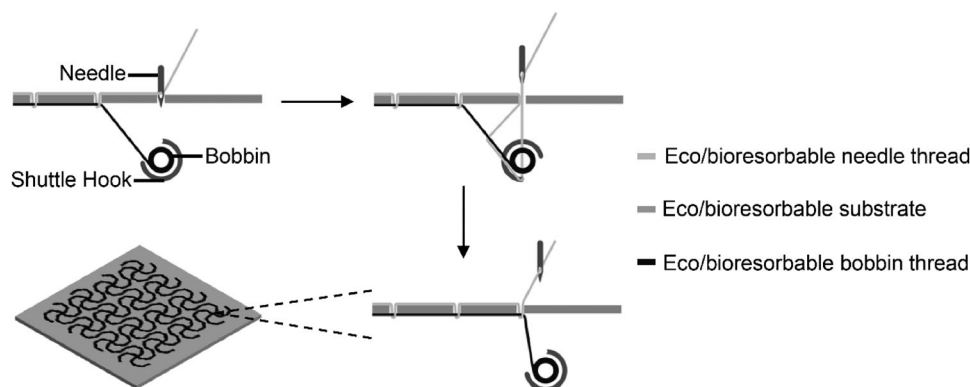
Y. Wu, G. Lee, Y. Wang, G. Wickerson, J.-K. Chang, J. Gu, Y. Zhang, J. Liu, Y. Huang, J. A. Rogers
 Querrey Simpson Institute for Bioelectronics
 Northwestern University
 Evanston, IL 60208, USA
 E-mail: jrogers@northwestern.edu
 E. Rytkin, Y. Wang, L. Tang, M. Madrid, I. R. Efimov, J. A. Rogers
 Department of Biomedical Engineering
 Northwestern University
 Evanston, IL 60208, USA
 M. Bimrose, S. Tawfick, W. P. King
 Department of Mechanical Science and Engineering
 University of Illinois Urbana-Champaign
 Urbana, IL 61801, USA

S. Li, Y. Huang, J. A. Rogers
 Department of Mechanical Engineering
 Northwestern University
 Evanston, IL 60208, USA
 Y. S. Choi
 Department of Materials Science and Engineering
 Yonsei University
 Seodaemun-gu, Seoul 03722, Republic of Korea
 G. Wickerson, J. A. Rogers
 Department of Materials Science and Engineering
 Northwestern University
 Evanston, IL 60208, USA
 J.-K. Chang
 Wearifi Inc
 Evanston, IL 60208, USA
 I. R. Efimov
 Department of Medicine
 Feinberg School of Medicine
 Northwestern University
 Chicago, IL 60611, USA

 The ORCID identification number(s) for the author(s) of this article can be found under <https://doi.org/10.1002/smll.202305017>

© 2023 The Authors. Small published by Wiley-VCH GmbH. This is an open access article under the terms of the Creative Commons Attribution License, which permits use, distribution and reproduction in any medium, provided the original work is properly cited.

DOI: 10.1002/smll.202305017



Scheme 1. Schematic illustration of the use of a sewing machine to fabricate eco/bioresorbable electronics.

materials are incompatible with the associated water/organic solvents and high-temperatures. Specialized methods must be developed.

Previous reports describe advanced schemes in transfer printing,^[8–11] physical vapor deposition through shadow masks,^[1,12,13] additive printing,^[14–18] and laser cutting/ablation.^[19–21] Each of these techniques has its own advantages and limitations. Transfer printing enables fabrication of devices for prototyping, but the complexity of the process may hinder its use in manufacturing. Deposition through shadow masks can be useful for certain steps in a fabrication sequence but operates most effectively only with thin layers of materials that can be evaporated.^[12] Additive printing of inks/paste through screens or nozzles provides complementary capabilities, with notable uses in patterning thick conductors for radio frequency (RF) applications.^[14] The most recent work in this area demonstrates that laser ablation, and associated commercial tools for that purpose, can pattern and structure wide-ranging classes of eco/bioresorbable conductors, semiconductors, and dielectrics.^[19] Disadvantages are in materials inefficiencies that follow from the subtractive nature of the mechanism and in expensive tooling that relies on picosecond pulsed lasers.

Sewing based on advanced systems from the textile industry represents a fast, low-cost, and well-established method for large-scale manufacturing of fabrics. The process avoids high temperatures and reactive solvents, as key advantages for uses in fabrication of eco/bioresorbable devices. Modern sewing machines are highly automated and capable of precise manipulation

of threads into complex patterns on fabric and polymeric substrates. Previous demonstrations in non-eco/bioresorbable electronics rely on copper wires,^[22] carbon nanotubes threads,^[23] metal-coated threads,^[24] conductive polymer-coated threads,^[25] and liquid metal fibers.^[26]

Here, we report an adaptation of this approach for use with eco/bioresorbable metal wires and polymeric filaments to embroider conductive traces on eco/bioresorbable substrates, in complex patterns and over large areas. Systematic studies explore different material options and operational parameters. Demonstrations include functional electronic components (e.g., stretchable interconnects, and inductive coils) and system-level examples, including stretchable and bioresorbable wireless pacemakers.

2. Results and Discussion

2.1. A Sewing Approach for Patterning Conductive Traces

Scheme 1 illustrates the automated, programmable sewing process for forming complex conductive patterns on thin, flexible substrates for applications in eco/bioresorbable electronics. A fine eco/bioresorbable metal wire and polymeric filament serve as the bobbin and needle thread, respectively. A polymeric film forms the eco/bioresorbable substrate. During operation, the needle penetrates the substrate to create a hole, through which the shuttle hook interlaces the needle thread with the bobbin thread inside the hole to form a lock stitch. Embroidery software controls the sewing/embroidery machine to generate patterns in desired geometries, in an automated fashion and at high speeds (e.g., 400 stitches per minute).

The images in **Figure 1a** show patterns formed using tungsten (W) wire (diameter: 50 μm) as the bobbin thread and polyvinyl alcohol (PVA) filaments as the needle thread. Examples include a serpentine mesh (Figure 1a-i) and a large-area (2.5 cm \times 2 cm) flower pattern (Figure 1a-ii) embroidered onto a film of PVA (thickness: 90 μm). This process also enables patterning of wires on both sides of the substrate (Figure 1a-iii). The separation between wires can be as small as 300 μm (Figure 1a-iv). These examples demonstrate feasibility for fabricating many other components as needed, such as branches from a bus line. As reported in detail elsewhere, both W and PVA are eco/bioresorbable.^[3,27–29] Accelerated tests highlight the various stages of an accelerated

J. A. Rogers
Department of Electrical and Computer Engineering
Northwestern University
Evanston, IL 60208, USA

J. A. Rogers
Department of Chemistry
Northwestern University
Evanston, IL 60208, USA

J. A. Rogers
Department of Neurological Surgery
Feinberg School of Medicine
Northwestern University
Chicago, IL 60611, USA

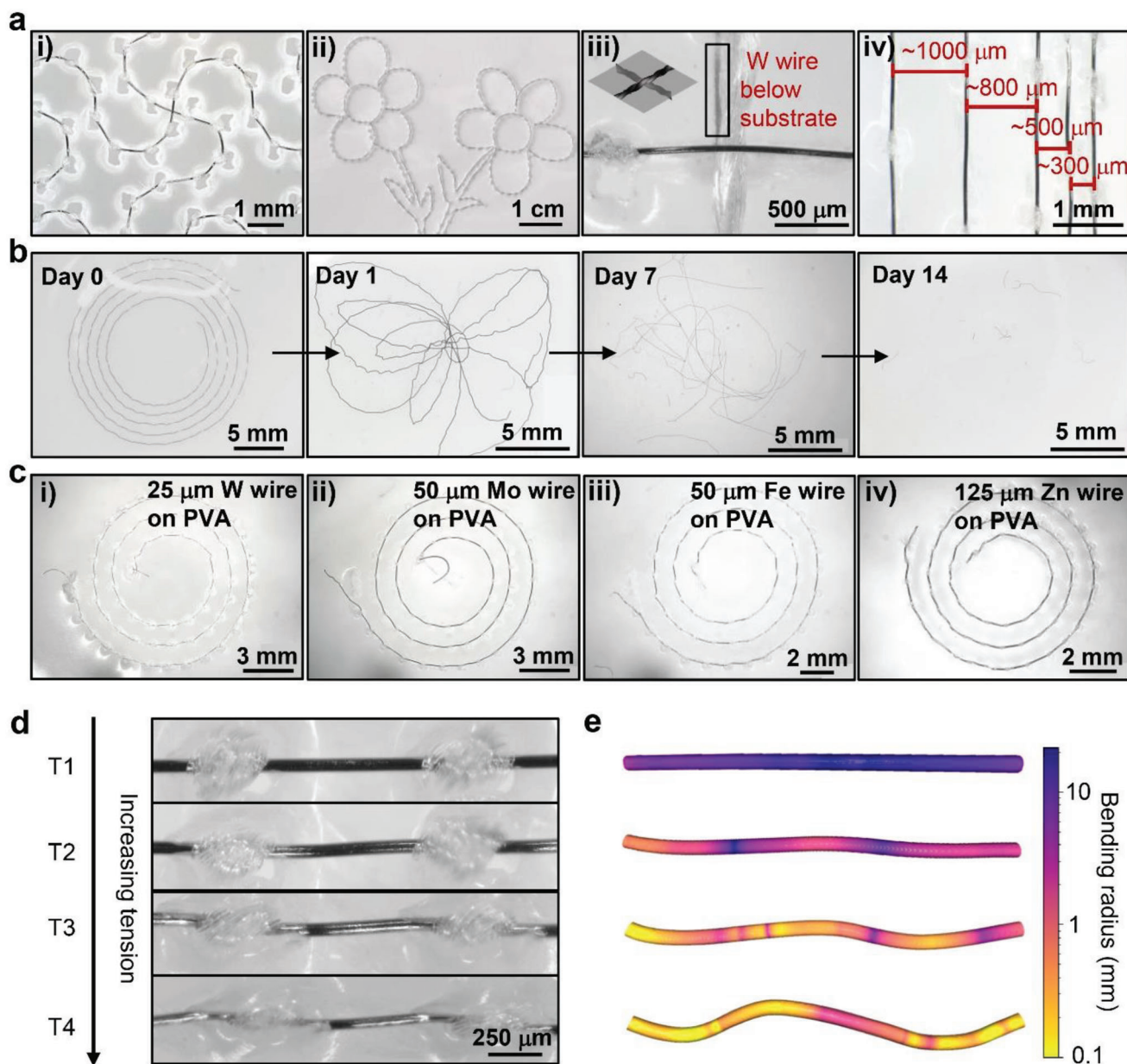


Figure 1. A sewing approach for patterning conductive traces. a) Images of patterns of i) a serpentine mesh, ii) a flower, iii) a criss-cross of metal wires at right angles, one above and one below the substrate (inset: schematic illustration of the crossover) and iv) parallel lines with varied separation spaces embroidered onto a film of polyvinyl alcohol (PVA) using W wire (diameter: 50 μm) as bobbin thread. b) Sequence of images that shows accelerated dissolution of a spiral pattern (50 μm W wire) embroidered onto a film of PVA in phosphate-buffered saline (PBS) solution (1 \times , pH 7.4) with 50×10^{-3} M H_2O_2 at 90 $^\circ\text{C}$ for 14 days. c) Images of spiral patterns embroidered onto a film of PVA (thickness: 90 μm) using i) W wire with a diameter of 25 μm , ii) Mo wire with a diameter of 50 μm , iii) Fe wire with a diameter of 50 μm , and iv) Zn wire with a diameter of 125 μm . d) Images of lines embroidered onto a film of PVA under varied tension settings. e) Three-dimensional-rendered computed tomography (CT) scans of the embroidered samples corresponding to Figure 1d.

resorption process for a spiral structure during immersion in phosphate-buffered saline (PBS) solution (1 \times , pH 7.4) with 50×10^{-3} M H_2O_2 at 90 $^\circ\text{C}$ (Figure 1b). The PVA substrate and PVA needle threads dissolve within 1 day, which leads to the disassembly of the spiral structure, leaving only the W wires. The wires subsequently react to form soluble tungstic ions through a series of hydrolysis reactions.^[30,31] The dissolution rate in this case depends on the chemical components in the surrounding aque-

ous environment. Immersion in simulated body fluids at physiological conditions (1 \times PBS solution, pH 7.4 at 37 $^\circ\text{C}$) for 131 days decreases the diameter of W wire from 51.5 ± 0.4 to 30.1 ± 0.5 μm and roughens the surface (Figure S1, Supporting Information). The rate is thus $\approx 60 \pm 1$ $\mu\text{m year}^{-1}$. Previous reports suggest rates of 200–500 $\mu\text{m year}^{-1}$ in aerated PBS solution (1 \times , pH 7.4) at room temperature, as extrapolated from electrochemical impedance spectroscopy data.^[30] The discrepancies likely arise

from the different measurement methods and the surrounding aqueous environment.

This sewing technique also applies to other eco/bioresorbable metals (e.g., molybdenum (Mo), iron (Fe), and zinc (Zn)), other diameters (e.g., 25, 35, and 125 μm) and polymeric films (e.g., poly-L-lactic acid (PLA), polycaprolactone (PCL), and poly(lactic-co-glycolic acid) (PLGA)) as in Figure 1c and Figure S2 (Supporting Information). The mechanical properties of the materials are important to consider. High-speed embroidery machines subject the threads to complex, dynamic mechanical conditions that involve tensile strains, bending deformations, frictional forces, shear stresses, and others. In particular, the tensile strength and bendability of the wires are key factors, closely related to the diameter and the type of metal. Typically, reducing the diameter increases the probability of fracture during the sewing process. For W wires used in the sewing machine studied here, the diameter can be as small as 25 μm (Figure 1c-i). Attempts with W wires of diameter $\approx 7.6 \mu\text{m}$ lead to frequent fractures. Mo and Fe wires with diameters of 50 μm are compatible with the sewing process (Figure 1c-ii and Figure 1c-iii). For wires of Zn and Mg alloys (WE22 alloy), however, diameters of 50 μm do not provide sufficient strength. Zn wires with diameters of 125 μm are acceptable (Figure 1c-iv).

An important parameter is the thread tension, defined by the force that pulls the thread between the needle and the bobbin. This tension determines the degree to which the thread penetrates the substrate, and it affects the final shape of the wires. Under high tension, the wires may tear through the edges of the holes in the substrate, resulting in local plastic deformation of the wires. Studies of this effect involve W wires sewn onto a PVA substrate with increasing tension using settings on the sewing machine (i.e., from 1 to 4) as a qualitative metric. X-ray computed tomography (CT) yields images of the resulting geometries of the stitches (Figure 1d,e). As expected, the degree of bending of the wires increases with tension. From the images, the minimum bending radius is 5.62, 0.94, 0.29, and 0.16 mm for tension settings 1 through 4, respectively. The corresponding maximum bending strain is 0.44%, 2.7%, 8.6%, and 15.6%, respectively. The yield strain of the W wire is $\approx 0.6\%$ (Figure S3, Supporting Information).

2.2. Fabrication of Stretchable Interconnects

Stretchable interconnects are essential in many eco/bioresorbable electronic systems, particularly those that require integration with soft, moving biological tissues.^[10,32,33] A common approach to stretchable interconnects relies on planar serpentine structures in metal traces formed on elastomeric substrates. This design converts stretching deformations to in and out of plane bending motions. Figure 2a shows the procedure for fabricating related types of stretchable interconnects using wires patterned by sewing. In this example, the first step involves sewing W wire onto a PVA substrate in serpentine configurations. A laser cutting process then removes PVA material from regions away from the wires, to form a corresponding serpentine ribbon of PVA with a width of 1 mm. Lastly, encapsulating the stitched serpentine interconnect between two layers of a bioresorbable polyurethane (PU) elastomer

completes the fabrication. The adhesion between these layers relies on thermally activated dynamic bond exchange reactions within the 3D network of the PU.^[32] The serpentine design in this case consists of half circles ($R = 1 \text{ mm}$) and straight lines ($L = 2 \text{ mm}$) (Figure S4, Supporting Information). The sewing process uses interlock stitches to fix the W wire into a bent status, leading to maximum strains in the W wire at the arc of the initial serpentine structure. The calculated maximum strain at the arc is 2.9%, which is beyond the yield strain ($\approx 0.6\%$) (Figure S3, Supporting Information) and thus corresponds to plastic deformation of the W wire. The W wire does not, as a result, recover its original straight shape after dissolving the PVA (Figure S5, Supporting Information). Figure 2b,c shows finite element analysis (FEA) results and optical images of the serpentine interconnect at various values of uniaxial strain, respectively. The color in the FEA results represents the effective strain in the material. The strains in the W wire initially concentrate on the arc regions, but with increasing stretching deformations, the serpentine structures unfold in a manner that decreases these strains.

Tests of these stretchable interconnects focus on changes in electrical resistance due to stretching deformations and to repeated cycles of stretch/release. Stretching to strains as high as 160%, corresponding to the breaking point of the serpentine structure, leads to no measurable changes in resistance (Figure 2d). The resistance also remains stable through 10 000 cycles of stretch/release to strains of 30% (Figure 2e). The serpentine structure fails, however, at ≈ 4000 cycles when tested in a similar manner up to strains of 40% as shown in Figure 2f. The fractures occur through both the wires and the PVA ribbons at the stitch point. A possible explanation is that holes in the PVA act as points of stress concentrations. Cracks that initiate at these locations then propagate under repeated cycles.^[34] The result causes complete fracture of the PVA ribbon, which further leads to stress concentrations on the portions of the W wire that coincide with the sites of PVA fracture, thereby leading to breakage of wire under repeated cycles due to metal fatigue. Support for this mechanism is in experiments that subject PVA serpentine structures with and without holes to 1000 cycles to strains of 50%. The structures with holes fracture, while those without do not (Figure S6, Supporting Information). This issue can be avoided by directly sewing W wires in serpentine configurations onto PU and then encapsulating with layers of PU above and below using the process described previously. The resulting structures exhibit negligible changes in resistance up to 160% strain and through 10 000 cycles of strains up to 60% (Figure S7, Supporting Information). After 1000 cycles of strains up to 80%, the wire breaks due to metal fatigue as shown on Figure S8 (Supporting Information).

2.3. Fabrication of Coil Antennas for Wireless data Communication and Power Transfer

RF coils are widely used as antennas in eco/bioresorbable electronics for wireless power transfer or/and data transmission via inductive magnetic coupling.^[35–37] Figure 3a shows images of two representative coils fabricated by sewing W wire onto a PVA substrate, as before. The diameters of the large and small coils are 45 and 20 mm, respectively. Both consist of 18 turns,

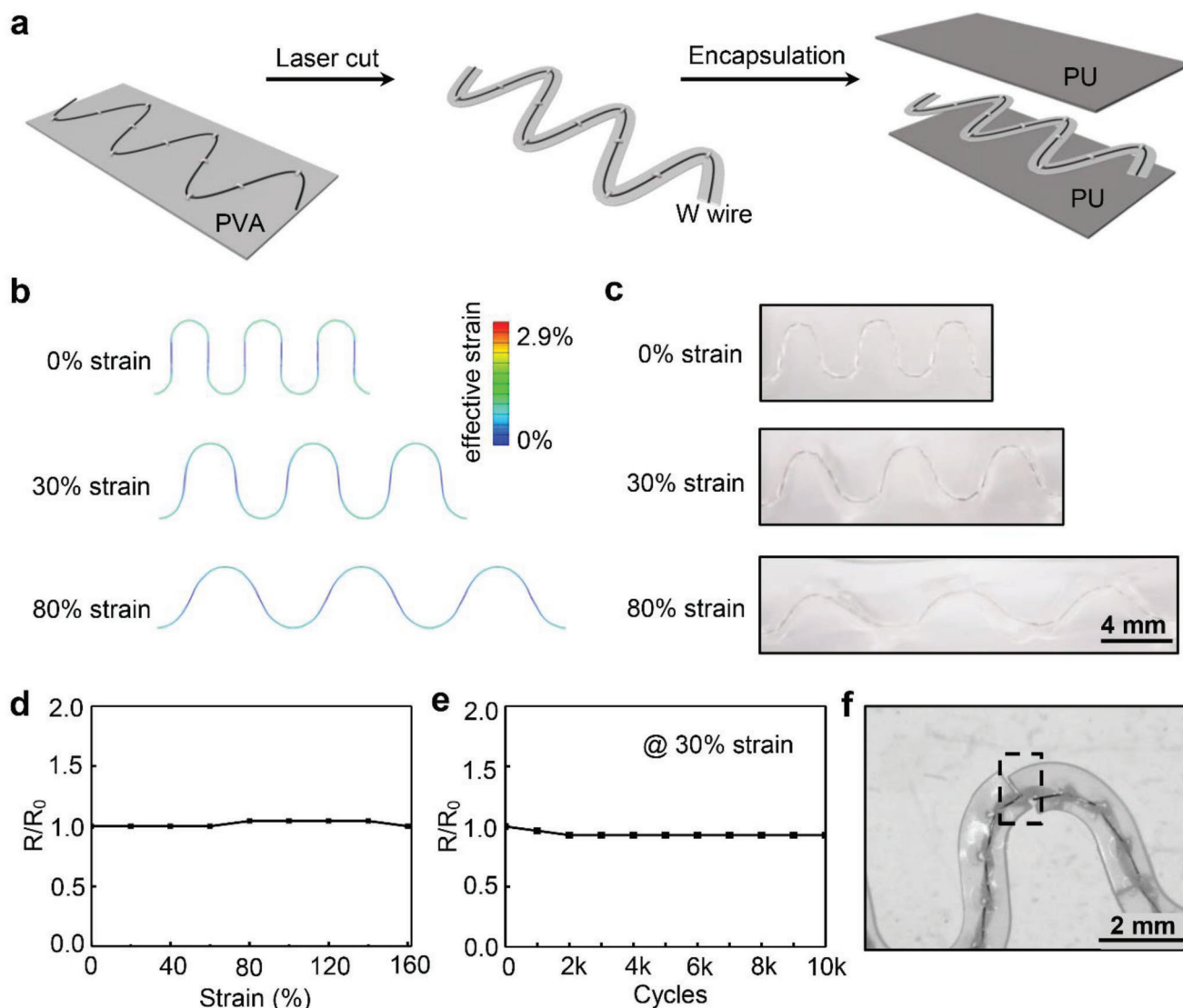


Figure 2. Fabrication of stretchable interconnects. a) Schematic illustration of the procedure for fabricating stretchable interconnects. b) Finite element analysis (FEA) results for the stretchable interconnect at various values of uniaxial strains. c) Images of the stretchable interconnects at various values of uniaxial strains. d) Plot of normalized resistance of the stretchable interconnect as a function of uniaxial stretching strain. e) Normalized resistance of the stretchable interconnect over 10 000 stretch-release cycles of 30% strain. f) Image showing fracture of the stretchable interconnect after ≈ 4000 stretch-release cycles of 40% strain.

with 1 mm and 0.5 mm spacings for the 45 and 20 mm coils, respectively. Figure 3b shows the results of measurements of the reflection coefficient S_{11} for these two coils. The resonant frequencies of the 45 and 20 mm coils are ≈ 50 and ≈ 150 MHz, respectively. Figure 3c shows an image of a coil encapsulated by PU, while wirelessly activating a light-emitting diode (LED) via inductive coupling to an external antenna (47×34 mm, four turns) powered with RF at a frequency of 13.56 MHz and a power of ≈ 1.7 W, located at the surface of the inductive antenna (NFC card reader expansion board X-NUCLEO-NFC06A1) (Figure 3d). This system operates stably in $1 \times$ PBS solution at a pH of 7.4 and temperature of 37°C , corresponding to physiological conditions, for over 20 days (Figure S9, Supporting Information). The PU encapsulation layer determines the lifetime of this device. PU

absorbs water with time and water dissolves PVA threads and films, leading to the change of the geometry of spiral structure of coils. These effects cause the resonance frequency of the coils to shift, thereby decreasing the transmission efficiency. The lifetime of the device could be extended by coating additional inorganic materials, such as SiO_2 , onto the PU encapsulation layer or by using an oil/polyanhydride structure as an encapsulation layer as recently reported in the literature.^[38] Replacing the LED with a radio-frequency identification (RFID) chip (NXP P60 chipset) yields an RFID tag, capable of wirelessly unlocking a car (Figure 3e,f). This system dissolves in PBS solution ($1 \times$, pH 7.4) with 50×10^{-3} M H_2O_2 at 90°C , leaving only the chip, which corresponds to $\approx 3\%$ of the total mass of the system (Figure S10, Supporting Information).

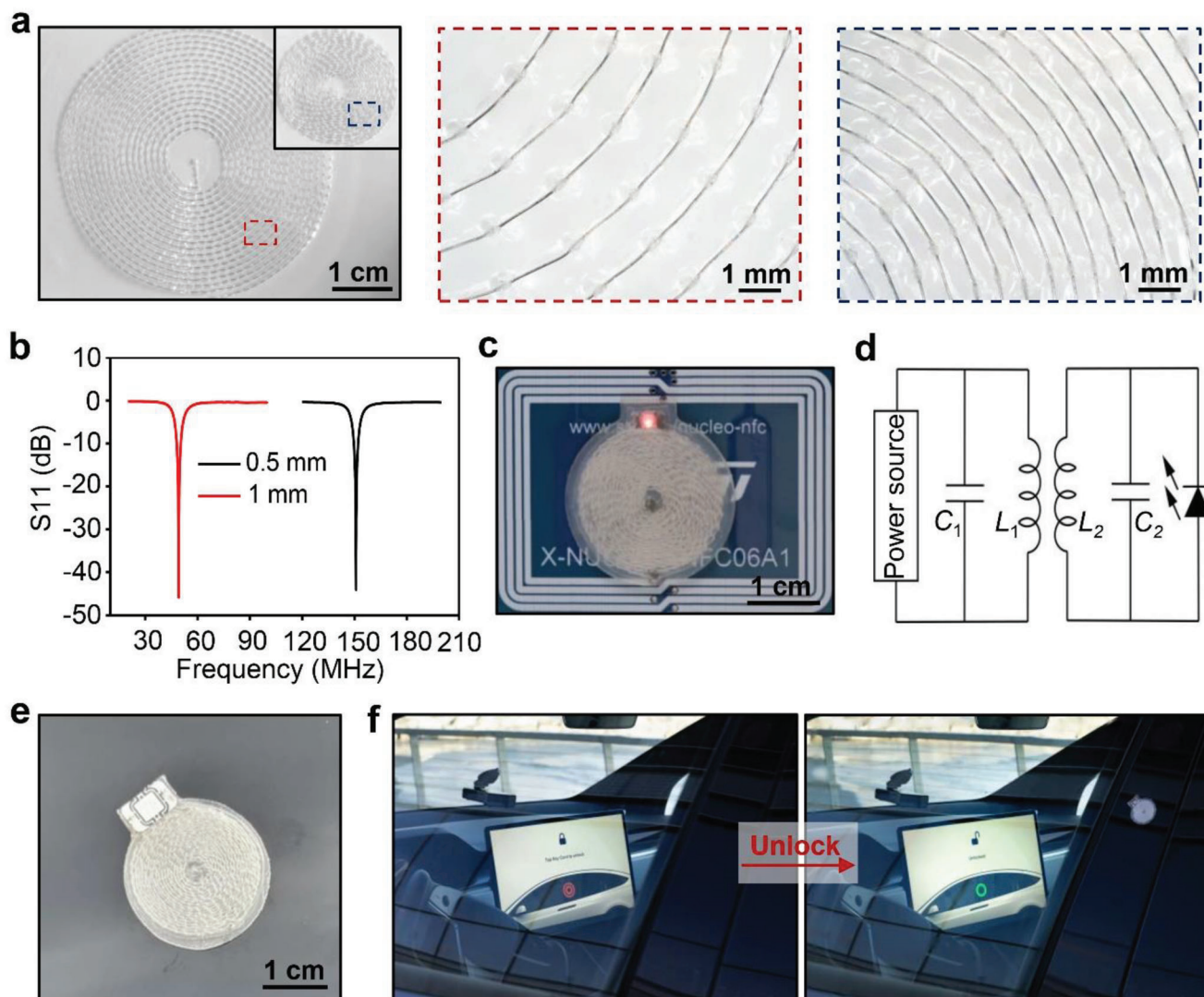


Figure 3. Fabrication of coil antennas for wireless data communication and power transfer. a) Images of spiral coils embroidered onto a film of polyvinyl alcohol (PVA) using 50 μm W wire. b) S11 parameter plot showing different peaks corresponding to different coils. c) Image of the sewn coil antenna to wirelessly power a red light-emitting diode. d) Schematic illustration of the circuit diagram for the transmission of radiofrequency power to light up a light-emitting diode. e) Image of a radio-frequency identification (RFID) tag fabricated by sewing. f) Images of an RFID tag to wirelessly unlock a car.

2.4. Fabrication of Stretchable, Wireless Pacemakers

Temporary pacemakers are useful for patients at risk for bradyarrhythmias during a recovery period of days or weeks after a cardiac surgery. Bioresorbable pacemakers for this application implant onto the epicardial surface at the final stages of the surgery before chest closure. Natural processes of bioresorption eliminate the need for surgical extraction procedures that can otherwise lead to complications when applied to the pacing leads of conventional temporary epicardial pacemakers.^[39] Stretchable, bioresorbable wireless epicardial pacemakers can be formed easily using the sewing techniques introduced here. **Figure 4a** shows an exploded view schematic illustration of such a device. The system consists of an RF-based wireless power-harvesting module and a pair of wire electrodes interconnected by a stretchable

serpentine structure. The wireless power-harvesting module includes two inductive coils separated by a thin film of PU as a dielectric interlayer. A PIN diode based on a doped monocrystalline silicon nanomembrane rectifies the RF power received by this module. A conductive composite paste of Candelilla wax and W microparticles serves as an electrical connection between the diode and coil. This same approach can be used as interconnects between different circuit layers. The wire electrode ties to a bioresorbable surgical suture using a knot, designed to fix the pacing electrodes to the heart and to prevent dislocation of the pacemaker. PU forms an encapsulating structure, as before, to isolate the active materials from the surrounding biofluids, thereby defining a period of stable operation aligned to clinical needs. **Figure 4b** shows an image of a device and a magnified view of the knot between the wire electrode and the bioresorbable suture.

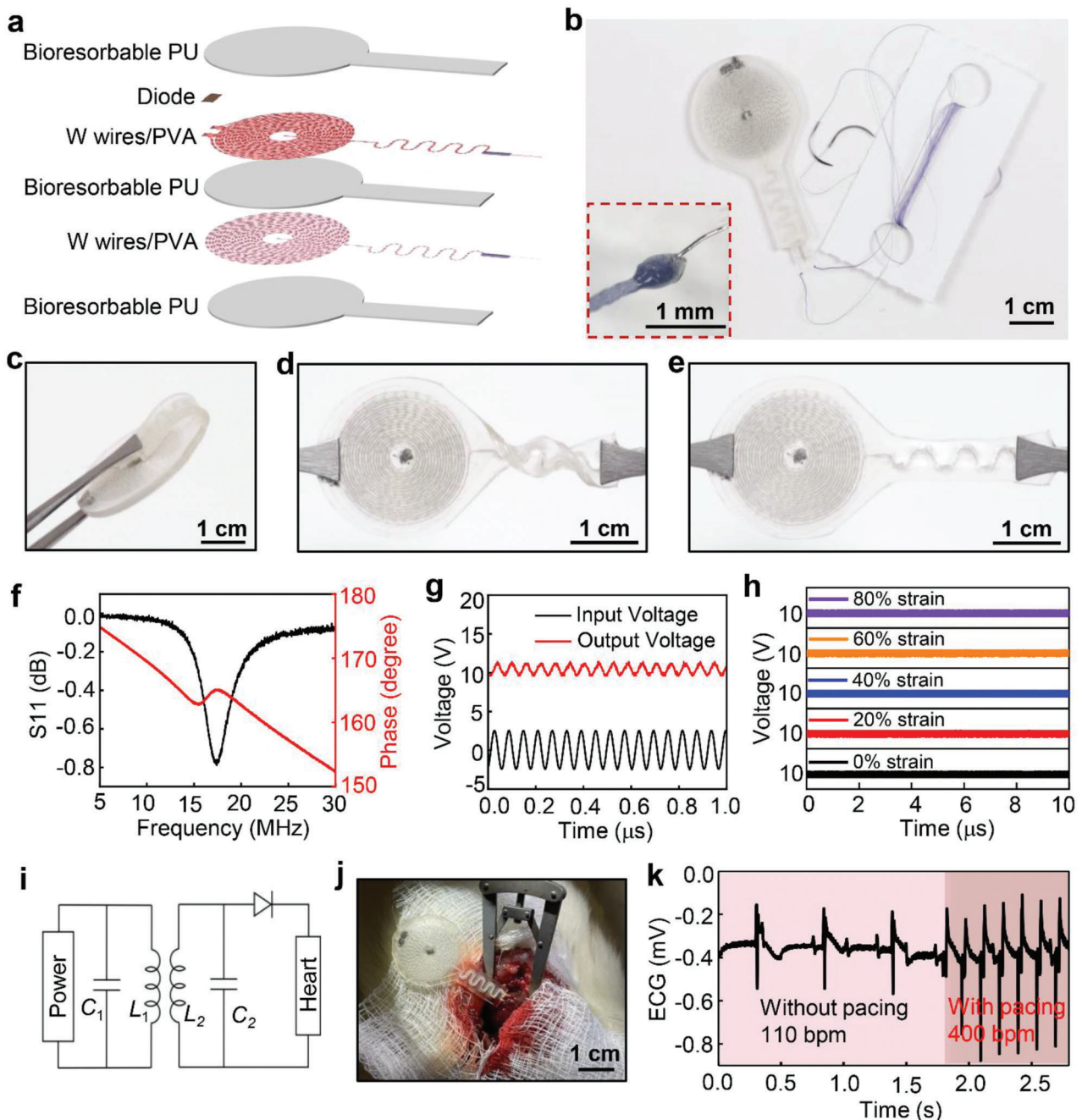


Figure 4. Fabrication of a stretchable, wireless pacemaker. a) Schematic illustration of the device design. b) Image of a device connected to a pair of surgical needles with 6-0 bioresorbable suture (inset: image of the knot between a W wire electrode and the suture). c–e) Images of a device subjected to c) folding (180°), d) twisting (360°), and e) stretching ($\approx 40\%$ strain). f) Plot of the S11 parameter versus frequency. g) Example of an output waveform generated by an alternating voltage applied to a transmission coil. h) Output open circuit voltage as a function of strain. i) Schematic illustration of the circuit diagram for the transmission of radiofrequency power to wirelessly pace the heart. j) Image of a stretchable, bioresorbable wireless pacemaker sutured onto the surface of a rat heart. k) Measured electrocardiograms (ECGs) of a rat with and without electrical simulation using a stretchable, bioresorbable wireless pacemaker.

The design provides high levels of mechanical robustness during folding (180°), twisting (360°), and stretching ($\approx 40\%$ strain) (Figure 4c–e).

Operation relies on inductive magnetic coupling between an external transmitter coil and the receiver coil of the pacemaker.

Figure 4f–h shows the electrical performance characteristics. The operating frequency is ≈ 17 MHz, within a range where absorption by biofluids and tissues is negligible (Figure 4f).^[40] Figure 4g presents the rectified monophasic open-circuit output (≈ 10 V) during wireless operation initiated by an external antenna

(diameter: 20 μm , 6 turns) powered with a sinusoidal alternating voltage waveform of ≈ 5 peak-to-peak voltage (V_{pp}) at a frequency of 17 MHz, located at the surface of the receiver coil of the pacemaker. The output voltage remains constant during mechanical deformation (Figure 4h). Accelerated tests demonstrate the resorption process associated with immersion in PBS solution (1 \times , pH 7.4) with 50×10^{-3} M H_2O_2 at 90 °C (Figure S11, Supporting Information).

In vivo evaluations using a rat model demonstrate the function of the device. RF power ($3 V_{pp}$) from a transmitter coil (diameter: 20 mm, 6 turns) near the receiver coil of the power-harvesting module of the pacemaker wirelessly delivers an electrical pulse with width of 2 ms that occurs every 150 ms to the myocardium of a heart via inductive coupling (Figure 4i). The wire electrodes insert inside the myocardium, secured using bioresorbable sutures (Figure 4j). Applying an electrical stimulus above a threshold value initiates cardiac excitation due to depolarization of the transmembrane potential. Figure 4k shows recordings of electrocardiograms (ECGs) before and after pacing. Successful ventricular capture pacing drives the heart rate from 110 to 400 bpm with shortened R–R intervals as expected.

3. Conclusion

In summary, the results presented here demonstrate the feasibility and applicability of a sewing technology approach to the fabrication of eco/bioresorbable stretchable interconnects, inductive coils and integrated systems for wireless light emitters, RFID tags and temporary cardiac pacemakers. These examples suggest many other opportunities in fabrication of eco/bioresorbable electronic devices, in ways that complement other reported schemes.

4. Experimental Section

Sewing Wires and Threads: Tungsten wires with diameters of 25, 35, and 50 μm were purchased from Midwest Tungsten Service. Mo wire (diameter: 50 μm), Fe wire (diameter: 50 μm), and Zn wire (diameter: 125 μm) were purchased from Goodfellow Corporation. Mg alloy (WE22 alloy) wire (diameter: 50 μm) was generously provided by Fort Wayne Metals. PVA threads (VanishLite) were purchased from Superior Threads and PVA films (thickness: 90 μm) were purchased from Smiththread. All wires/threads were used as received.

Embroidery Processes with Eco/bioresorbable Metal Wires: Design patterns including lines, spiral coils, serpentine structure, and flowers were digitized to a stitch trajectory using a commercial software package (Hatch Embroidery 3, Wilcom). The stitch length could be changed and optimized using this Embroidery software. A computerized sewing/embroidery machine (SE600, Brother) with a maximum embroidery area of 10 \times 10 cm was used to embroider the metal wires onto film substrates with PVA threads as needle threads and metal wires as bobbin threads. PVA films were mainly selected as substrates to demonstrate the fabrication capability of the sewing due to their low-cost and commercial availability.

CT Scans of the Stitched Samples and Bending Radius Calculations: The sewn structures were measured using a Xradia Bio MicroCT machine. Each scan took approximately 2 h with a 2 μm voxel size and a grid size of 1009 \times 989 \times 988. The W wire was isolated in the 3D data by using a binary threshold to remove data artifacts, resulting in no observable change in the measured wire shape. The boundary surface for the 3D wire was computed by slicing the volume along the x , y , and z dimensions, performing Canny edge detection on the binary data slices, and combining the extracted edge

data.^[41] The stitch medial axis was calculated using methods inspired by the Vascular Modeling Toolkit library for modeling and analyzing blood vessels.^[42] Using the boundary surface point cloud, this work created a weighted graph that included the center line of the stitch using a Voronoi diagram and Delaunay tessellation. The shortest path between ends of the stitch along the graph nodes created an accurate approximation for the center line of the stitch in 3D space.^[43] This work next smoothed the stitch centerline $c(s)$ and derived the radius of curvature and torsion in the wire using the finite difference method to calculate derivatives between consecutive data points.^[44] The curvature is defined as

$$\kappa(s) = \frac{|c'(s) \times c''(s)|}{|c'(s)|^3} \quad (1)$$

and measures the deviation of the stitch from a straight line. The bending radius was calculated for each discrete location in the wire by calculating the inverse of the curvature $1/\kappa(s)$.

Fabrication and Characterization of Stretchable Serpentine Interconnects: A serpentine pattern of W wires (diameter: 50 μm) was embroidered onto a PVA substrate. A laser cutter (LPKF ProtoLaser R) was used to remove PVA material from regions away from the wires, to form a corresponding serpentine ribbon of PVA with a width of 1 mm. Encapsulating the embroidered serpentine W wire between two layers of PU completed the fabrication of the stretchable serpentine interconnect. Methods for preparing PU films appear elsewhere.^[32] Each interconnect sample was clamped at its two ends and stretched, while connected to a multimeter to record the resistance at different strains. For evaluation of the reliability, the structures were stretched and released at a frequency of 1 Hz. The resistance was recorded after each 1000 cycles.

FEA of Stretchable Serpentine Interconnects: 3D FEA was performed by the commercial software Abaqus to study the deformations and strain distributions of W wires under different stretching strains. Eight-node 3D solid elements were employed, and mesh convergence was tested to ensure computational accuracy. A straight W wire was first modeled, and certain points were fixed at specific locations in a PVA substrate to simulate the sewing process. A stretching strain was then applied to the substrate to study the deformation. The elastic modulus (E) and Poisson's ratio (ν) are $E_W = 410$ GPa and $\nu_W = 0.28$ for W and $E_{PVA} = 35$ MPa and $\nu_{PVA} = 0.49$ for PVA.

Fabrication and Characterization of Stretchable, Bioresorbable Wireless Pacemakers: Coils and serpentine structures of W wires (diameter: 50 μm) were embroidered in a PVA film (thickness: 90 μm). Laser cutting removed excess PVA to define the outline of the coil and serpentine structure. A PIN diode was electrically connected to the coil using a biodegradable conductive W paste. PIN diodes and the biodegradable conductive W paste were fabricated as described previously.^[32,45] Thin layers of PU were used as a spacer between the two layers of coil and serpentine structure and as top and bottom encapsulation. Hot pressing the entire system at 200 °C completed the fabrication. For devices used for surgical implantation, a pair of bioresorbable sutures (Veterinary Sutures Vet-Cryl Polyglactin 6-0) with surgical needles were tied to the wire electrodes of the pacemaker using a knot. The knot and the rest of the structure were partially planarized by a coating of polyhydride to minimize the shear forces associated with tissue contact. The polyhydride was synthesized as described previously.^[46] The scattering parameter S11 of the device was characterized using a network analyzer (Agilent E5062A, Keysight) connected with a single-turn coil by a coaxial cable. The RF power was from the function generator (Agilent 33250A 80 MHz). The output voltage from the wire electrodes was measured using an oscilloscope (BK Precision 100 MHz).

Surgical Procedures for Cardiac Pacing: The procedure to implant the bioresorbable pacemaker via open thoracotomy was adapted from that described in a previous report.^[47] ≈ 12 -week-old Sprague–Dawley male rats were used for the tests. The surgical space was prepared according to the approved animal protocol by the Northwestern University Institutional Animal Care and Use Committee (IS00021087), which included the preparation of an induction chamber, intubation station, surgical workspace, ventilator, surgical instrument and equipment area, adjustable lights, and

a heating bed. General anesthesia was induced by inhaling isoflurane vapors with 3–4% isoflurane in an induction chamber. The loss of consciousness was confirmed with a toe pinch. The path of vaporized isoflurane was switched to an intubation stand. The rat's tongue was gently retracted, and the vocal cords were visualized. The cannula was blindly passed, supported by a blunt curved stylet, through the vocal cords into the trachea. The proper placement of the endotracheal tube was confirmed. The ventilator was connected, and pressure-mode ventilation was selected with 80 breaths per minute and a peak inspiratory pressure limit of 14 cm H₂O. The intubated animal was placed on a heating pad and prepared for surgery. A 4 × 4 cm area was shaved and disinfected with a 10% povidone-iodine solution, followed by alcohol wipes. Subdermal ECG electrodes were placed in the Lead II configuration. The curvilinear dissection was made with surgical scissors over the chest 2 cm below the left axilla. The dissection was carried through the skin and muscle layer until the ribs and muscle layer were directly visualized. During the incision, the bleeding was stopped by applying direct pressure or electrocautery. A small animal retractor was inserted to help visualize the heart surface. The pericardium was opened and cleared using forceps and cotton swabs. The pacemaker electrodes were secured onto the heart surface utilizing the sutures with careful positioning not to engage the coronary arteries.

Supporting Information

Supporting Information is available from the Wiley Online Library or from the author.

Acknowledgements

This work made use of the Keck-II facility and the NUFAB facility of Northwestern University's NUANCE Center, which has received support from the SHyNE Resource (NSF ECCS-2025633), the IIN, and Northwestern's MRSEC program (NSF DMR-1720139). Engineering efforts were supported by the Querrey Simpson Institute for Bioelectronics at Northwestern University.

Conflict of Interest

The authors declare no conflict of interest.

Data Availability Statement

The data that support the findings of this study are available from the corresponding author upon reasonable request.

Keywords

eco/bioresorbable electronic devices, eco/bioresorbable metal wires, eco/bioresorbable stretchable interconnects, embroidery, wireless stretchable pacemaker

Received: June 14, 2023

Revised: July 15, 2023

Published online: August 1, 2023

- [1] S. W. Hwang, H. Tao, D. -H. Kim, H. Cheng, J. -K. Song, E. Rill, M. A. Brenckle, B. Panilaitis, S. M. Won, Y. -S. Kim, Y. M. Song, K. J. Yu, A. Ameen, R. Li, Y. Su, M. Yang, D. L. Kaplan, M. R. Zakin, M. J. Slepian, Y. Huang, F. G. Omenetto, J. A. Rogers, *Science* **2012**, 337, 1640.

- [2] W. B. Han, J. H. Lee, J. -W. Shin, S. -W. Hwang, *Adv. Mater.* **2020**, 32, 2002211.
- [3] K. K. Fu, Z. Wang, J. Dai, M. Carter, L. Hu, *Chem. Mater.* **2016**, 28, 3527.
- [4] G. D. Cha, D. Kang, J. Lee, D. -H. Kim, *Adv. Healthcare Mater.* **2019**, 8, 1801660.
- [5] K. Rajaram, S. M. Yang, S. -W. Hwang, *Adv. Energy Sustainability Res.* **2022**, 3, 2100223.
- [6] R. Jamshidi, M. Taghavimehr, Y. Chen, N. Hashemi, R. Montazami, *Adv. Sustainable Syst.* **2022**, 6, 2100057.
- [7] H. -J. Yoon, G. Lee, J. -T. Kim, J. -Y. Yoo, H. Luan, S. Cheng, S. Kang, H. L. T. Huynh, H. Kim, J. Park, J. Kim, S. S. Kwak, H. Ryu, J. Kim, Y. S. Choi, H. -Y. Ahn, J. Choi, S. Oh, Y. H. Jung, M. Park, W. Bai, Y. Huang, L. P. Chamorro, Y. Park, J. A. Rogers, *Sci. Adv.* **2022**, 8, eade3201.
- [8] S. -W. Hwang, D. -H. Kim, H. Tao, T. -i. Kim, S. Kim, K. J. Yu, B. Panilaitis, J. -W. Jeong, J. -K. Song, F. G. Omenetto, J. A. Rogers, *Adv. Funct. Mater.* **2013**, 23, 4087.
- [9] S. -W. Hwang, J. -K. Song, X. Huang, H. Cheng, S. -K. Kang, B. H. Kim, J. -H. Kim, S. Yu, Y. Huang, J. A. Rogers, *Adv. Mater.* **2014**, 26, 3905.
- [10] S. -W. Hwang, C. H. Lee, H. Cheng, J. -W. Jeong, S. -K. Kang, J. -H. Kim, J. Shin, J. Yang, Z. Liu, G. A. Ameer, Y. Huang, J. A. Rogers, *Nano Lett.* **2015**, 15, 2801.
- [11] J. -K. Chang, H. Fang, C. A. Bower, E. Song, X. Yu, J. A. Rogers, *Proc. Natl. Acad. Sci. U. S. A.* **2017**, 114, E5522.
- [12] A. Palmroth, T. Salpavaara, P. Vuoristo, S. Karjalainen, T. Kaariainen, S. Miettinen, J. Massera, J. Leikkala, M. Kellomaki, *ACS Appl. Mater. Interfaces* **2020**, 12, 31148.
- [13] A. Palmroth, T. Salpavaara, J. Leikkala, M. Kellomki, *Adv. Mater. Technol.* **2019**, 4, 1900428.
- [14] X. Huang, Y. Liu, S. -W. Hwang, S. -K. Kang, D. Patnaik, J. F. Cortes, J. A. Rogers, *Adv. Mater.* **2014**, 26, 7371.
- [15] B. K. Mahajan, X. Yu, W. Shou, H. Pan, X. Huang, *Small* **2017**, 13, 1700065.
- [16] Y. K. Lee, J. Kim, Y. Kim, J. W. Kwak, Y. Yoon, J. A. Rogers, *Adv. Mater.* **2017**, 29, 1702665.
- [17] A. Zareei, V. Selvamani, S. Gopalakrishnan, S. Kadian, M. K. Maruthamuthu, Z. He, J. Nguyen, H. Wang, R. Rahimi, *Adv. Mater. Technol.* **2022**, 7, 2101722.
- [18] K. -S. Kim, J. Yoo, J. -S. Shim, Y. -I. Ryu, S. Choi, J. -Y. Lee, H. M. Lee, J. Koo, S. -K. Kang, *Adv. Mater. Technol.* **2021**, 7, 2001297.
- [19] Q. Yang, Z. Hu, M. -H. Seo, Y. Xu, Y. Yan, Y. -H. Hsu, J. Berkovich, K. Lee, T. -L. Liu, S. McDonald, H. Nie, H. Oh, M. Wu, J. -T. Kim, S. A. Miller, Y. Jia, S. Butun, W. Bai, H. Guo, J. Choi, A. Banks, W. Z. Ray, Y. Kozorovitskiy, M. L. Becker, M. A. Pet, M. R. MacEwan, J. -K. Chang, H. Wang, Y. Huang, J. A. Rogers, *Nat. Commun.* **2022**, 13, 6518.
- [20] J. Koo, M. R. MacEwan, S. -K. Kang, S. M. Won, M. Stephen, P. Gamble, Z. Xie, Y. Yan, Y. -Y. Chen, J. Shin, N. Birenbaum, S. J. Chung, S. B. Kim, J. Khalifeh, D. V. Harburg, K. Bean, M. Paskett, J. Kim, Z. S. Zohny, S. M. Lee, R. Zhang, K. Luo, B. Ji, A. Banks, H. M. Lee, Y. Huang, W. Z. Ray, J. A. Rogers, *Nat. Med.* **2018**, 24, 1830.
- [21] H. Guo, D. D'Andrea, J. Zhao, Y. Xu, Z. Qiao, L. E. Janes, N. K. Murthy, R. Li, Z. Xie, Z. Song, R. Meda, J. Koo, W. Bai, Y. S. Choi, S. W. Jordan, Y. Huang, C. K. Franz, J. A. Rogers, *Adv. Funct. Mater.* **2021**, 31, 2102724.
- [22] R. Rahimi, M. Ochoa, W. Yu, B. Ziaie, *J. Micromech. Microeng.* **2014**, 24, 095018.
- [23] L. W. Taylor, S. M. Williams, J. S. Yan, O. S. Dewey, F. Vitale, M. Pasquali, *Nano Lett.* **2021**, 21, 7093.
- [24] T. Linz, C. Kallmayer, R. Aschenbrenner, H. Reichl, in *Proc. Ninth IEEE Int. Symp. on Wearable Computers*, IEEE, Osaka, Japan **2005**, pp. 86–89.
- [25] S. Darabi, M. Hummel, S. Rantasalo, M. Rissanen, I. O. Mansson, H. Hille, B. Hwang, M. Skrifvars, M. M. Hamed, H. Sixta, A. Lund, C. Muller, *ACS Appl. Mater. Interfaces* **2020**, 12, 56403.
- [26] R. Lin, H. -J. Kim, S. Achavananthadith, Z. Xiong, J. K. W. Lee, Y. L. Kong, J. S. Ho, *Nat. Commun.* **2022**, 13, 2190.

- [27] H. Ryu, M. -H. Seo, J. A. Rogers, *Adv. Healthcare Mater.* **2021**, *10*, 2002236.
- [28] L. Yin, H. Cheng, S. Mao, R. Haasch, Y. Liu, X. Xie, S. -W. Hwang, H. Jain, S. -K. Kang, Y. Su, R. Li, Y. Huang, J. A. Rogers, *Adv. Funct. Mater.* **2014**, *24*, 645.
- [29] C. Fernandes, I. Taurino, *Sensors* **2022**, *22*, 3062.
- [30] E. Patrick, M. E. Orazem, J. C. Sanchez, T. Nishida, *J. Neurosci. Methods* **2011**, *198*, 158.
- [31] A. S. Idil, N. Donaldson, *J. Neural Eng.* **2018**, *15*, 021006.
- [32] Y. S. Choi, Y. -Y. Hsueh, J. Koo, Q. Yang, R. Avila, B. Hu, Z. Xie, G. Lee, Z. Ning, C. Liu, Y. Xu, Y. J. Lee, W. Zhao, J. Fang, Y. Deng, S. M. Lee, A. Vazquez-Guardado, I. Stepien, Y. Yan, J. W. Song, C. Haney, Y. S. Oh, W. Liu, H. -J. Yoon, A. Banks, M. R. MacEwan, G. A. Ameer, W. Z. Ray, Y. Huang, T. Xie, et al., *Nat. Commun.* **2020**, *11*, 5990.
- [33] Y. S. Choi, H. Jeong, R. T. Yin, R. Avila, A. Pfenniger, J. Yoo, J. Y. Lee, A. Tzavelis, Y. J. Lee, S. W. Chen, H. S. Knight, S. Kim, H. -Y. Ahn, G. Wickerson, A. Vazquez-Guardado, E. Higbee-Dempsey, B. A. Russo, M. A. Napolitano, T. J. Holleran, L. A. Razzak, A. N. Miniovich, G. Lee, B. Geist, B. Kim, S. Han, J. A. Brennan, K. Aras, S. S. Kwak, J. Kim, E. A. Waters, et al., *Science* **2022**, *376*, 1006.
- [34] R. M. Christensen, *Appl. Mech. Rev.* **2023**, *75*, 030801.
- [35] H. Li, F. Gao, P. Wang, L. Yin, N. Ji, L. Zhang, L. Zhao, G. Hou, B. Lu, Y. Chen, Y. Ma, X. Feng, *ACS Appl. Mater. Interfaces* **2021**, *13*, 21067.
- [36] S. -W. Hwang, X. Huang, J. -H. Seo, J. -K. Song, S. Kim, S. Hage-Ali, H. -J. Chung, H. Tao, F. G. Omenetto, Z. Ma, J. A. Rogers, *Adv. Mater.* **2013**, *25*, 3526.
- [37] D. Lu, Y. Yan, Y. Deng, Q. Yang, J. Zhao, M. -H. Seo, W. Bai, M. R. MacEwan, Y. Huang, W. Z. Ray, J. A. Rogers, *Adv. Funct. Mater.* **2020**, *30*, 2003754.
- [38] G. Lee, M. D. Does, R. Avila, J. Kang, K. D. Harkins, Y. Wu, W. E. Banks, M. Park, D. Lu, X. Yan, J. U. Kim, S. M. Won, A. G. Evans, J. T. Joseph, C. L. Kalmar, A. C. Pollins, H. Karagoz, W. P. Thayer, Y. Huang, J. A. Rogers, *Adv. Sci.* **2023**, 2301232, <https://doi.org/10.1002/advs.202301232>.
- [39] A. S. Batra, S. Balaji, *Ann. Pediatr. Cardiol.* **2008**, *1*, 120.
- [40] E. Cocherova, J. Surda, J. Pucik, V. Stofanik, in *Proc. 19th Int. Conf. Radioelektronika*, IEEE, Bratislava, Slovakia **2009**, pp. 327–329.
- [41] D. J. McGregor, M. V. Bimrose, S. Tawfick, W. P. King, *J. Mater. Process. Technol.* **2022**, *306*, 117605.
- [42] L. Antiga, M. Piccinelli, L. Botti, B. Ene-Iordache, A. Remuzzi, D. A. Steinman, *Med. Biol. Eng. Comput.* **2008**, *46*, 1097.
- [43] T. K. Dey, W. Zhao, in *Proc. of the 7th ACM Symposium of Solid Modeling Applications. SMA'02*, ACM, New York **2002**, pp. 356–366.
- [44] M. Piccinelli, A. Veneziani, D. A. Steinman, A. Remuzzi, L. Antiga, *IEEE Trans. Med. Imaging* **2009**, *28*, 1141.
- [45] S. M. Won, J. Koo, K. E. Crawford, A. D. Mickle, Y. Xue, S. Min, L. A. McIlvried, Y. Yan, S. B. Kim, S. M. Lee, B. H. Kim, H. Jang, M. R. MacEwan, Y. Huang, R. W. Gereau, J. A. Rogers, *Adv. Funct. Mater.* **2018**, *28*, 1801819.
- [46] Y. S. Choi, J. Koo, Y. J. Lee, G. Lee, R. Avila, H. Ying, J. Reeder, L. Hambitzer, K. Im, J. Kim, K. -M. Lee, J. Cheng, Y. Huang, S. -K. Kang, J. A. Rogers, *Adv. Funct. Mater.* **2020**, *30*, 2000941.
- [47] R. T. Yin, S. W. Chen, K. B. Lee, Y. S. Choi, J. Koo, Q. Yang, M. A. Napolitano, J. Ausra, T. J. Holleran, J. B. Lapiano, E. A. Waters, A. Brikha, G. Kowalik, A. N. Miniovich, H. S. Knight, B. A. Russo, A. Kiss, A. Murillo-Berlioz, T. Efimova, C. R. Haney, P. Gutruf, J. A. Rogers, G. D. Trachiotis, I. R. Efimov, *Nat. Protoc.* **2023**, *18*, 374.